

Ashkan Nazari¹

Center for Tire Research (CenTiRe), Department of Mechanical Engineering, Virginia Tech, Blacksburg, VA 24061 e-mail: nazari@vt.edu

Lu Chen

Computational Research for Energy Systems and Transport (CREST) Lab, Department of Mechanical and Aerospace Engineering, University at Buffalo, Buffalo, NY 14260 e-mail: luchen90@vt.edu

Francine Battaglia

Computational Research for Energy Systems and Transport (CREST) Lab, Department of Mechanical and Aerospace Engineering, University at Buffalo, NY 14260 e-mail: fbattagl@buffalo.edu

John B. Ferris

Vehicle Terrain Performance Laboratory, Department of Mechanical Engineering, Virginia Tech, Blacksburg, VA 24061 e-mail: jbferris@vt.edu

Gerardo Flintsch

Center for Sustainable Transportation Infrastructure, Virginia Tech Transportation Institute, Blacksburg, VA 24061 e-mail: gflintsch@vtti.vt.edu

Saied Taheri

Center for Tire Research (CenTiRe), Department of Mechanical Engineering, Virginia Tech, Blacksburg, VA 24061 e-mail: staheri@vt.edu

Prediction of Hydroplaning Potential Using Fully Coupled Finite Element-Computational Fluid Dynamics Tire Models

Hydroplaning is a phenomenon that occurs when a layer of water between the tire and pavement pushes the tire upward. The tire detaches from the pavement, preventing it from providing sufficient forces and moments for the vehicle to respond to driver control inputs such as breaking, accelerating, and steering. This work is mainly focused on the tire and its interaction with the pavement to address hydroplaning. Using a tire model that is validated based on results found in the literature, fluid-structure interaction (FSI) between the tire-water-road surfaces is investigated through two approaches. In the first approach, the coupled Eulerian-Lagrangian (CEL) formulation was used. The drawback associated with the CEL method is the laminar assumption and that the behavior of the fluid at length scales smaller than the smallest element size is not captured. To improve the simulation results, in the second approach, an FSI model incorporating finite element methods (FEMs) and the Navier-Stokes equations for a two-phase flow of water and air, and the shear stress transport k-w turbulence model, was developed and validated, improving the prediction of real hydroplaning scenarios. With large computational and processing requirements, a grid dependence study was conducted for the tire simulations to minimize the mesh size yet retain numerical accuracy. The improved FSI model was applied to hydroplaning speed and cornering force scenarios. [DOI: 10.1115/1.4047393]

Keywords: fluid-structure interaction, CFD, tire, hydroplaning

1 Introduction

Hydroplaning is a key issue for safe driving on wet roadways, and depends on vehicle velocity, water film thickness (WFT), tire construction, tread pattern, etc. Hydroplaning is more probable when the volume of the water in contact with the tire is more than the ability of the tire to expel the water. When the tire velocity reaches the hydroplaning speed, the force caused by the fluid pressure at the water–tire interface lifts the tire from the pavement. The risk of a vehicle accident when the pavement is wet is much more considerable than for dry conditions. Statistics from different regions of the world show that nearly 20% of traffic accidents happen on wet roads [1]. Detailed information regarding the exact reasons for accidents during wet road conditions is not available.

However, hydroplaning and low skid resistance are considered as the main factors leading to traffic accidents [2]. Accordingly, hydroplaning has become an important field of study in the automotive and tire industries as they try to address the factors affecting vehicle hydroplaning. Since it is expensive and difficult to create conditions in a laboratory environment that induce hydroplaning, multiphysics modeling and computer simulations are used to study the onset of hydroplaning.

Albert [3] discussed the effects of tire design parameters on hydroplaning and showed that the most important factor is geometric design of the tread pattern. Using a three-region concept, Albert concluded that as the vehicle speed increased, the dynamic water pressure increased at the front edge of the tire and completely lifted the tire, leading to hydroplaning. Initial studies on hydroplaning have been mostly focused on physical experiments and empirical methods. Recently, improvements with computer resources have provided opportunities to solve complex problems and there have been efforts devoted to developing computer codes to study hydroplaning.

^{*}Corresponding author.

Contributed by the Fluids Engineering Division of ASME for publication in the JOURNAL OF FLUIDS ENGINEERING. Manuscript received October 6, 2019; final manuscript received April 19, 2020; published online June 26, 2020. Assoc. Editor: Ning Zhang.

Hydroplaning involves the reactions when a layer of water impedes perfect contact between the tire and the road. Fluid-structure interaction (FSI) is the interaction of a moving deformed structure with fluid flow, and can be used to model hydroplaning. FSI is an important and interesting phenomenon, but because it poses challenges for numerical modeling, several methods are utilized to solve FSI problems, such as the finite element method (FEM) and the explicit finite volume method. Matthies and Steindorf [4] presented a theoretical study of FSI in which the strengths and weaknesses of coupling FSI solvers were discussed. The displacement responses of weak and strong couplings were compared, and based on a numerical evaluation of the Jacobian for the complete system of equations obtained using separate solvers, a strong coupling approach was proposed. In the work by Walhorn et al. [5], a strong coupling method was presented for an FEM solver developed by the authors. In their approach, weak coupling problems due to time-marching schemes and exchanging information were formulated and solved simultaneously at each time-step. The approach considered a nonlinear Lagrangian motion for the structure and a mixed Lagrangian–Eulerian formulation for the fluid. Kim and Jeong [6] applied a combination of finite differencing and an finite element (FE) tire model to iteratively predict the onset of hydroplaning. They compared approaches for a full-iteration method, a oneiteration method, and no-iteration method, and determined that the hydroplaning speeds of a straight-grooved tire predicted using the one-iteration method was almost the same as that obtained from the full-iteration method.

In a study that incorporated fluid motion, Vincent et al. [7] used a generalized formulation of the Navier-Stokes equations for a two-phase flow to simulate the interaction between the air-water flow and the tire. However, it is known that the flow experienced during hydroplaning is largely turbulent in nature and should be considered. Ong and Fwa [8] indicated that the $k-\varepsilon$ turbulence model can be used for flows at high- or near-hydroplaning speeds. The k- ε turbulence model is the simplest turbulence model but may not properly predict complex flows involving severe pressure gradients, separation, and strong streamline curvature [9,10]. Guo et al. [11] selected the renormalization group $k-\varepsilon$ model since it can successfully predict high strain-rate flows and large bending fluid streamlines. Zhou et al. [12] chose the shear stress transport (SST) k-ω model because it has advantages for a range of Reynolds number (Re) flows by combining features of two turbulence models. The standard k- ω model is used in the inner boundary layer providing the ability as a low-Re turbulence model near surfaces, and the $k-\varepsilon$ model is used in the outer boundary layer, thus improving the predictive capabilities [10,13]. The hydroplaning flow also involves two or more immiscible fluids, such as air, water, and water vapor. Most researchers [2,12,14-19] presented computational fluid dynamics (CFD) results using the volume of fraction (VOF) multiphase flow model by solving a single set of momentum equations and tracking the volume fraction of each fluid throughout the domain.

Several studies used commercial finite element codes to predict hydroplaning for different conditions, employing approaches such as the arbitrary Lagrangian-Eulerian and coupled Eulerian-Lagrangian (CEL) methods [20-25]. However, these studies only solved the single-phase fluid as an Eulerian fluid element assuming inviscid, laminar flow. The assumption of inviscid flow ignores the effect of shear stress and the laminar assumption simplifies hydroplaning behavior, thus neglecting the presence of turbulence. In addition, modeling fluids as an Eulerian element is not computationally practical since the fluid solution is dependent on the mesh size and requires the element size to be extremely small to resolve the fluid length scale. However, using CFD can better capture the free surface flow with moving boundaries to build and track the amount of water as well as the volume fraction of other fluids with the VOF model. The overarching technical challenge is to accurately simulate hydroplaning using FSI techniques without restrictive assumptions such as inviscid, laminar flow.

In this work, hydroplaning is investigated using two FSI methods. The first method solves both structure and fluid using the structural solver within ABAQUS with the CEL formulation. The second method uses STAR-CCM+ to model the two-phase turbulent flow of water and air, and the solutions are coupled with ABAQUS to model the tire deformation. First, the ABAQUS-CEL hydroplaning model is verified using empirical relations developed by NASA [26]. Second, the CFD approach is validated and numerical accuracy is determined to ensure grid-independent solutions. Next, the effect of hydrodynamic forces at different speeds is lower than the critical hydroplaning speed, and the corresponding cornering forces at different slip angles are presented for both FSI approaches and compared with experimental data in the literature. It is shown that the proposed hydroplaning modeling approaches are able to capture the effect of water on the net force as well as tire concerning force. A significant contribution of this work is that the authors demonstrate the importance of including CFD models for turbulence and two-phase flow with finite element analysis (FEA) models to capture the hydrodynamics of water and the tire. Besides the agreement, this work also shows the differences between the two FSI approaches using ABAQUS-CEL and ABAQUS-STAR-CCM+ coupling due to different assumptions of viscous flow and free water surface tracking through tire splash interaction.

2 Numerical Methodology

The main models considered for the theoretical foundations of the hydroplaning simulations include the tire model, the fluid flow model, and the coupling between the two.

2.1 Tire Modeling. There are three methods that can be used to model a rolling tire: implicit dynamic, arbitrary Lagrangian-Eulerian, and dynamic explicit models [27]. For tire modeling at dry and wet condition, different physics based and numerical models are introduced to predict the tire force [28–30]. As shown in Fig. 1, first the two-dimensional (2D) cross section of the tire including the reinforcements is modeled. Next, the single pitch tread is added and the rim is mounted. In the next step, using the symmetric model generation capability in ABAQUS, the threedimensional (3D) full tire model is generated in which a tread pitch is periodically repeated to create 360 deg of a full tire model. At this step, all of the loads, including inflating the tire and the normal load, are applied. Finally, the contact between the tire tread and pavement is defined, and using a steady-state transport analysis, the overall rolling analysis is completed. The results from steady-state rolling step are exported into a transient rolling step to evaluate the effect of the force due to WFT on the tire through cosimulation with CFD code. Equation (1) shows the tire deformation for displacement field u

$$\nabla \sigma(u) + b = \rho \ddot{u} \tag{1}$$

 ρ is the mass density, b is the body force, and σ is the Cauchy stress

2.2 Tire Materials Modeling. The composite materials used to create a tire structure are very complex making it difficult to predict the material behavior. The tire components that are made of rubber include the tread, sidewall, apex, and inner liner. Therefore, large elastic deformation theory is implemented into the model [31–33] to ensure good predictions. With regard to the importance of the materials modeling, the neo-Hookean hyperelastic model is utilized for its ability to reasonably represent the hyper-elastic characteristics of rubber. A list of the equations used for the hyper-elastic materials model and the corresponding properties are presented in Tables 1 and 2.

In this work, a 180/65 R 15 steel belted radial tire is used for hydroplaning analysis. For the tire components, different element types are used to reflect the real characteristics of the tire

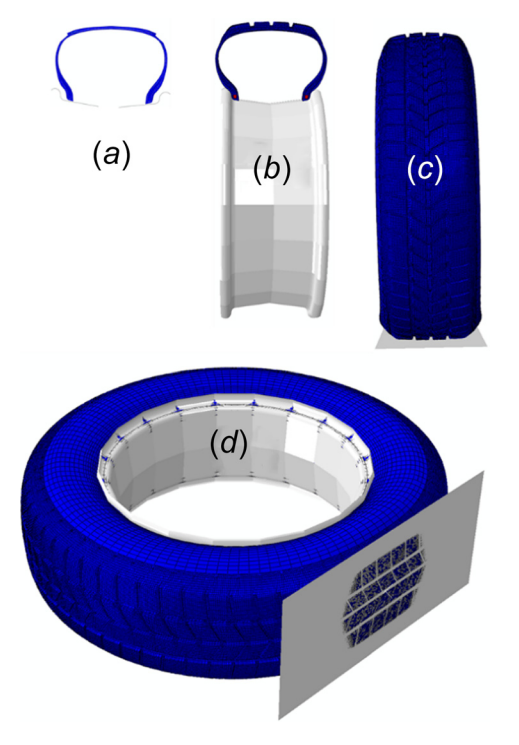


Fig. 1 Tire modeling procedure in ABAQUS: (a) cross section and reinforcements modeling, (b) rim mounting and tread implementation, (c) load applying and foot print analysis, and (d) steady-state rolling analysis

components. The belt and ply in 2D use the ABAQUS embedded element SFMGAX1, and in 3D the ABAQUS element SFM3D4R is used. For all other tire components such as the carcass, sidewall, and tread, in 2D, the ABAQUS element CGAX4R and in 3D, the ABAQUS element C3D8R are employed. In addition, for both road surface and rim, an analytical surface is utilized.

2.3 Fluids Modeling Using Computational Fluid Dynamics. The commercial software STAR-CCM+ is employed for the CFD work and provides the advantage for FSI with the capability to couple with ABAQUS for the FE modeling. For the fluid flow, the Navier–Stokes equations are applied coupled with turbulence and multiphase flow models. The fundamental equations of fluid dynamics are based on conservation of mass (continuity), momen-

 $\frac{\partial \overline{\rho}}{\partial t} + \nabla \cdot \left(\overline{\rho} \, \overline{v} \, \right) = 0 \tag{2}$

$$\frac{\partial}{\partial t} \left(\overline{\rho} \, \overline{v} \, \right) + \nabla \cdot \left(\overline{\rho} \, \overline{v} \, \overline{v} \, \right) = -\nabla p + \rho \mathbf{g} + \nabla \cdot \overline{\overline{\tau}} \tag{3}$$

$$\frac{\partial}{\partial t}(\overline{\rho}E) + \nabla \cdot \left[\overline{v} \, \left(\rho E + p \right) \right] = \nabla \cdot k_{\rm eff} \nabla T + \nabla \cdot \left(\overline{\overline{\tau}}_{\rm eff} \cdot \overline{v} \, \right) \quad (4)$$

Table 1 The equations used for neo-Hookean model

Eq	uation

$$W = f(I_1, I_2, I_3)$$

$$I_1 = \lambda_1^2 + \lambda_2^2 + \lambda_3^2$$

$$I_2 = \lambda_1^2 \lambda_2^2 + \lambda_2^2 \lambda_3^2 + \lambda_3^2 \lambda_1^2$$

$$I_3 = \lambda_1^2 \lambda_2^2 \lambda_3^2$$

$$W = C_{10} (\overline{I_1} - 3) + \frac{1}{D_1} (\overline{J_{e1}} - 3)^2$$

tum, and energy, shown as

Table 2 Material properties of the tire components

Element	C10 (MPa)	D1 (2/MPa)
Carcass	0.446	0.045
Sidewall	0.318	0.063
Rim strip	0.930	0.021
Belt	1.022	0.019
Tread	0.685	0.029
Apex	3.512	0.006

where p is the pressure, \mathbf{g} is the gravitational field, $\bar{\bar{\tau}}$ is the fluid stress tensor, \overline{v} is the fluid velocity vector, E is the total energy, and $k_{\rm eff}$ and $\bar{\bar{\tau}}_{\rm eff}$ are the effective thermal conductivity and effective stress tensor, respectively. The mean density $\overline{\rho}$ corresponds to the volume-fraction-averaged density used in the multiphase flow model, which is described in Sec. 2.3.1.

2.3.1 Two-Phase Flow Modeling. The VOF is used to model water and air, and their flow surrounding the tire, such as splash, spray, and wind effects, by tracking the volume fraction of each fluid throughout the domain. The volume fraction of all phases must sum to unity, which means that the variables and properties in a given cell are purely a representation of one of the phases, or representative of a mixture, depending on the volume fraction. If the volume fraction $\phi = 1$, the cell is full of the primary fluid (e.g., water) while if the value is 0, the cell is full of the secondary fluid (e.g., air). For volume fractions between 0 and 1, the cell contains an interface between the primary and secondary fluids. The tracking of the interface between the phases can be accomplished by solving the conservation of mass equation for the volume fraction of one or more phases. To track sharp interfaces, the convective terms of the volume fraction transport equation are discretized using a high resolution interface capturing scheme [34]. For the primary phase, the equation is

$$\frac{\partial \phi}{\partial t} + v \cdot \nabla \phi = 0 \tag{5}$$

where ϕ represents the space occupied by each phase (water and air) and mass and momentum conservations are specified by each phase individually, where the water and air volume fractions sum to one

$$\phi_w + \phi_a = 1 \tag{6}$$

The fluid density in Eqs. (2)–(4) is solved as the volume-fraction-averaged density, which in each cell is given by

$$\overline{\rho} = \phi_w \rho_w + (1 - \phi_w) \rho_a \tag{7}$$

where ρ_w is the water density and ρ_a is the air density.

2.3.2 Shear Stress Transport $k-\omega$ Turbulence Model. The SST $k-\omega$ model has been coupled in the CFD model for its ability to predict the onset and flow separation from surfaces [13]. The SST $k-\omega$ model combines the advantages of both the $k-\omega$ turbulence model the $k-\varepsilon$ turbulence model to predict the boundary layer and the freestream flow. The SST $k-\omega$ model gradually transitions from the standard $k-\omega$ model in the inner region of the boundary layer to a high-Reynolds-number version of the $k-\varepsilon$ model in the outer part of the boundary layer [13].

The advantage is that other $k-\varepsilon$ turbulence models do not account for the transport of the turbulent shear stress, thus overpredicting the eddy-viscosity. The proper transport behavior can be obtained by using a limiter to the formulation of the eddy-viscosity

$$\mu_{t} = \frac{\rho k}{\omega} \frac{1}{\max\left[\frac{1}{\alpha}, \frac{SF_{2}}{\alpha\omega}\right]}$$
(8)

where S is the strain rate magnitude and α is the damping coefficient for turbulent viscosity causing low-Reynolds number correction. The turbulence kinetic energy k and the specific dissipation rate ω are solved numerically from the following transport equations using the SST $k-\omega$ model:

$$\frac{\partial}{\partial t}(\overline{\rho}\,k) + \nabla \cdot \left(\overline{\rho}\,k\,\overline{v}\,\right) = \nabla \cdot \left(\Gamma_k \nabla k\right) + G_k - Y_k \tag{9}$$

$$\frac{\partial}{\partial t}(\overline{\rho}\,\omega) + \nabla \cdot (\overline{\rho}\,\omega\,\overline{\nu}\,) = \nabla \cdot (\Gamma_{\omega}\nabla\omega) + G_{\omega} - Y_{\omega} \tag{10}$$

where G_k represents the generation of turbulence kinetic energy due to mean velocity gradients, G_{ω} is the generation of specific dissipation rate ω , Γ is the effective diffusive, Y_k and Y_{ω} represent the dissipation of k and ω due to turbulence.

2.3.3 Computational Domain and Boundary Conditions. To analyze the water flow field in the tire grooves during tire—ground contact, the shape of the deformed tire must be known. The assumption of the tire deformation was simplified according to theoretical and experimental work (see, e.g., Refs. [35–41]). However, other researchers [12] used the extraction of a deformed tread shape in the tire deformation FE model [12] and acquired the deformation with the wheel load. In the work herein, the computational mesh size was determined by balancing the accuracy for representing the hydrodynamics and tire dynamics with reasonable computational processing demands.

Figure 2 illustrates the computational domain and boundary conditions with deformed tire geometry extracted from FEM to capture the fluid dynamics, aerodynamics, and interactions with the moving tire. The domain is 2 m long in the direction of the moving tire, 80 cm tall and 60 cm wide. The 180/65 R 15 steel belted radial tire has a diameter $D_{\rm tire} = 61.5\,{\rm cm}$ and width $W_{\rm tire} = 18$ cm. The initial wheel spindle position was located at 30 cm to account for the tire deformation using an average vehicle weight of 1633 kg (3600 lb). The spindle position was used as the reference point such that the tire rotates with angular velocity ω_Y , equal to the ratio between the vehicle speed $V_{\rm tire}$ and tire radius R_{tire} . The Reynolds number (Re) for hydroplaning can be calculated using the vehicle speed and tire width by defining $Re = \rho_w$ $V_{\rm tire} \ W_{\rm tire} / \mu_{\rm w}$, where $\mu_{\rm w}$ is the water dynamic viscosity. A typical Reynolds number for the inception of hydroplaning (assuming a vehicle speed of 15 m/s) is 2.4×10^6 . Therefore, the work herein has been modeled assuming turbulent flow.

The boundary conditions have been specified to represent, as closely as possible, a realistic hydroplaning scenario. A layer of water that represents the water film thickness enters at the front

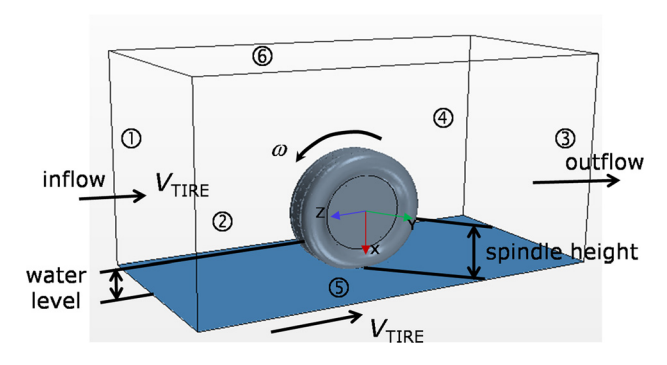


Fig. 2 Schematic of the computation domain (2 m \times 80 cm \times 60 cm) used in star-ccm+

plane of the computational domain (labeled "inflow" 1) in Fig. 2. The air and water are defined with the relative velocity magnitude, which is the same as the vehicle speed but in the opposite direction of the moving tire. The pavement is also specified with the same relative velocity magnitude in the z-direction. Water enters an area defined by the water level height (WFT = 5 mm) and the width of surface ① with a uniform velocity corresponding to the vehicle speed V_{tire} . Above the water film, air enters the remaining area of surface @ with a uniform velocity $V_{\rm tire}$. The pavement (surface ⑤) is defined as a no-slip wall boundary condition with the same relative velocity. The rear computational plane ("outflow" 3) specifies atmospheric pressure equal to 0 gauge pressure. The tire is modeled as a no-slip surface with no axial velocity but a constant angular velocity, corresponding to the rotating speed in the FE model. To reduce the effects of ambient boundaries that define the flow field, the two side surfaces (2) and (a) and the top surface (b) of the computational domain are specified as a free-slip boundaries with zero shear stress.

The geometry of the tire is imported from the FE tire model (see Secs. 2.1 and 2.2) and then remeshed in STAR-CCM+ with the fluid domain included. The tire mesh and contact patch is shown in Fig. 3(a) and the overall mesh of the fluid model is shown in Fig. 3(b). Polyhedral cells were created to ensure sufficient grid resolution to capture the fine details of the tire tread and capture the fluid impact on the tire. The "advancing layer mesher" has been employed to generate layers of prismatic cells around the tire structure and fill the remaining voids with polyhedral cells. The advantage of this surface mesh method is that each side of the interface can be mapped/matched conformally. To save computational time, along the pavement, the mesh gets coarser with the cell size increase by a ratio of 1.3.

2.4 Fluid-Structure Coupling. Fluid-structure interaction is achieved by coupling the FEM and the explicit finite volume method, which provides stable convergence, while other approaches can generate oscillations and can even produce unstable behaviors. Arbitrary thin structures can be handled by the model, including nonlinear effects such as the contact between rigid and flexible walls [42]. The coupling between the CFD model and ABAQUS model in STAR-CCM+ transfers information between the fluid model and tire model. An outline of the algorithm and coupling approach are shown in Fig. 4. The coupling exchanges time-dependent data such as pressure and nodal coordinates during tire deformation between the CFD and FE solvers. Using direct cosimulation coupling results in more efficient data transfer compared to the use of an external "MIDDLEWARE" software.

2.5 Coupled Eulerian-Lagrangian Method in ABAQUS. The cosimulation approach using STAR-CCM+ (Sec. 2.4) will be compared with the conventional CEL method, which utilizes both Eulerian and Lagrangian approaches. The CEL method has been shown to be highly efficient compared to the physics-based models when the interaction between tire and water or soil is studied [43]. The Eulerian domain is shaped to capture the fluid motion, whereas the Lagrangian approach tracks the movement of the structure as well represents the interface between the fluid and structure. At each time increment, the Eulerian domain is recreated and new boundaries are shaped. To do so, computed volume fractions from the Eulerian elements are used [44]. In the ABAQUS CEL approach, the tire displacement is solved instead of the velocity. To prevent the elements from dramatically deforming, the Lagrangian mesh is remapped using the original Eulerian mesh through interpolation. Although the method assumes that the fluid is compressible in the Navier-Stokes equations, a very high bulk module is used to approximate an incompressible fluid. The governing conservation equations for mass and momentum solved in CEL are

$$\frac{D\rho}{Dt} + \rho \nabla \cdot \frac{Dd}{Dt} = 0 \tag{11}$$

$$\rho \frac{D^2 d}{Dt^2} - \rho g - \nabla . \sigma = 0 \tag{12}$$

where g is the gravity, d is the displacement, and σ is the Cauchy stress tensor that is related to the equation of state (EOS). As shown in Eqs. (11) and (12), the displacement will be solved instead of velocity. Also, the Mie–Gruneisen form of EOS is used in ABAQUS defining the relation between pressure and density

$$p - p_H = \Gamma \rho (e - E_H) \tag{13}$$

where p_H , E_H , and e are the Hugoniot pressure, Hugoniot-specific energy per unit mass, and energy density, respectively, which are functions of density only. U

sing Eq. (13) decouples the energy equation from the continuity and momentum equations whereby pressure is only function of density $p = p(\rho)$ and not a function of the energy density. For the case of hydroplaning, the EOS for water is simplified

$$p = p_0 c_0^2 \left(1 - \frac{\rho_0}{\rho} \right) \tag{14}$$

where constants c_0 and ρ_0 are obtained from experimental data.

The aforementioned assumptions can be the origin of errors associated with the conventional CEL method for which the

cosimulation approach correctly models. For further details regarding the CEL method, readers are referred to Refs. [44–47].

3 Results and Discussion

3.1 Grid Convergence Study. A grid resolution study is conducted for a bald tire in both FSI approaches, in terms of the overall lift force. The lift forces calculated on the tire surface are computed as

$$f = \sum \left(\overrightarrow{f^p} + \overrightarrow{f^s} \right) \cdot \overrightarrow{n_f} \tag{15}$$

where f is the vertical component of the tire force, superscripts p and s are the pressure and shear force, respectively, acting on the tire surface, and n_f is the vertical unit vector. The pressure force and the shear force on the tire surface are computed as

$$\overrightarrow{f^p} = \left(\overrightarrow{P} - \overrightarrow{P_{\text{ref}}}\right) \overrightarrow{A_t}$$
 (16)

$$\overline{f^s} = -\overrightarrow{T}_f \ \overline{A}_t \tag{17}$$

where P_{ref} is the reference pressure, A_t is the tire face area, and the T_f is the stress tensor exerted on the tire surface area by the fluid combination of air and water.

The grid convergence index (GCI) methodology [22] is used to determine the numerical accuracy of the solutions for each grid

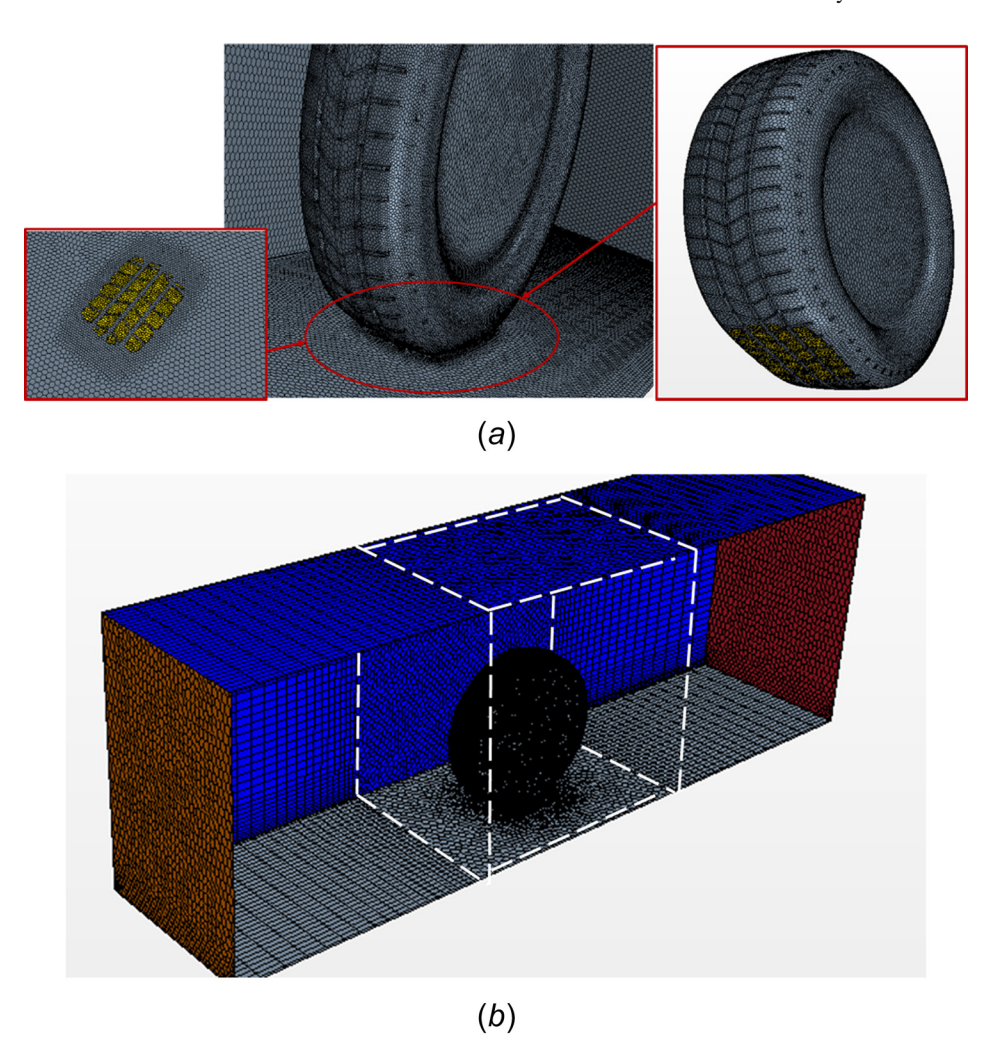


Fig. 3 Mesh profile of the CFD computational domain: (a) mesh detail of the CFD tire model and (b) mesh detail of the whole fluid domain

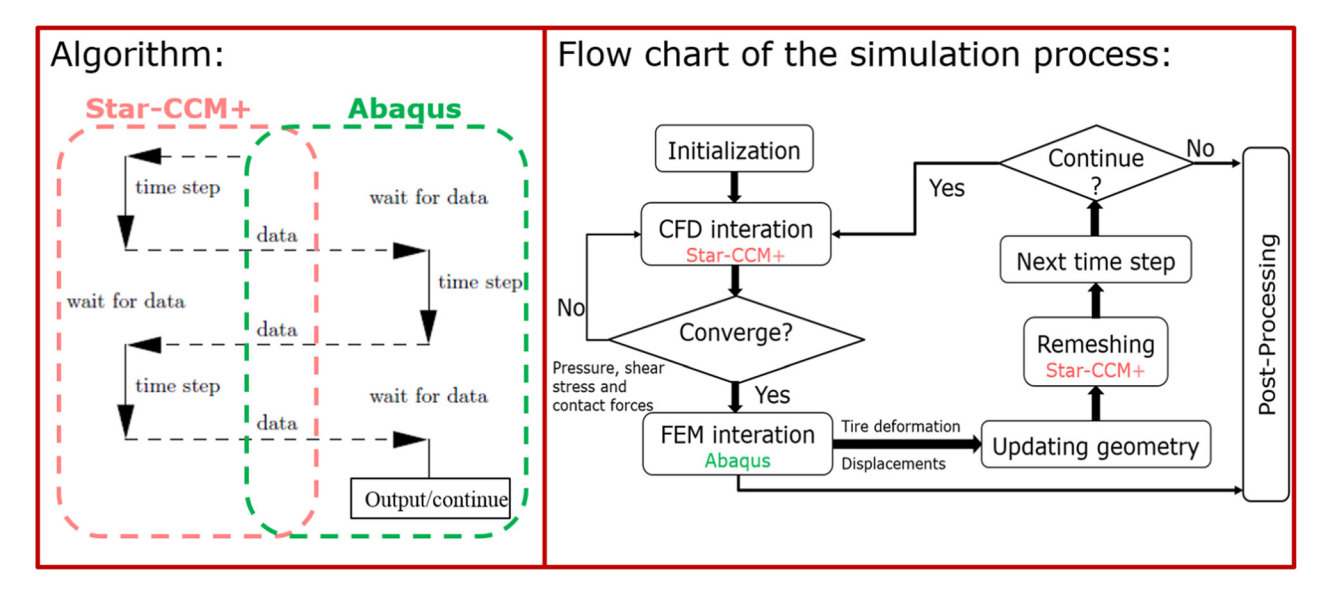


Fig. 4 FSI two-way coupling scheme

resolution and quantify errors that are caused from discretization or truncation in the CFD simulations [48]. The bald tire is studied under a 2100 N weight load with high tire pressure. The tire speed is 17.9 m/s with 5 mm water film thickness. Three mesh densities are selected with the base sizes of h_1 , h_2 , and h_3 for the fine, medium, and coarse meshes, respectively, shown in Table 3. The base size is the core characteristic dimension of the grid cell. The meshing refinement function has been kept the same for the three tested cases. The total cell numbers for three mesh densities in STAR-CCM+ are 1.58×10^6 , 5.10×10^5 , and 1.48×10^5 . Also, the total cell numbers for the three mesh densities in ABAQUS CFD are 1.575×10^6 , 4.70×10^5 , and 1.39×10^5 .

Figure 5 compares the pressure on the bald tire for the coarse, medium and fine grid resolutions in STAR-CCM+. It is evident that with increasing grid resolution, the effects of the pressure are more resolved. Further details related to the pressure distribution will be discussed with Fig. 6. To quantify the GCI, the total lift forces have been calculated at a quasi-steady condition with physical time of 0.04 s, in Table 3. The comparison of the total lift forces for the three grid resolutions reveals that the lift forces share similar magnitudes in both methods. The global apparent order of accuracy, P, in the GCI method in STAR-CCM+ and ABAQUS CFD is 4.54 and 3.21, respectively. The GCI values for the predicted total lift forces from the cosimulation of STAR-CCM+ and ABAQUS are 8.4% and 1.4% for the coarse-medium and mediumfine grids, respectively. Also, the GCI values for the predicted total lift forces in ABAOUS-CEL are 6.3% and 1.6% for the coarsemedium and medium-fine grids, respectively (the full GCI results are given in Table 3). Based on the GCI values, it is obvious that the refinement of the mesh improves the numerical accuracy significantly. To maintain consistent accuracy and to ensure sufficient mesh density to capture the details of the tire tread for the cosimulation in START-CCM+, the fine base size 0.02 m was used for the remainder of the study for the tread and half tread tire simulations. Applying the same meshing refinement function, the tread tire simulations use 2.73×10^6 grid cells. It is noteworthy to mention that since the fluid Eulerian domain in ABAQUS Explicit of CEL method can move with the tire in the longitudinal direction, it is possible to utilize a smaller CFD domain around the tire compared to computational domain in STAR-CCM+.

3.2 Model Verification. The critical hydroplaning speed $v_{\rm cr}$ can be used to verify the computational predictions of the CFD-FE cosimulation (Sec. 2.4) and the CEL model (Sec. 2.5) with

empirical relations and published experiments. The NASA empirical equation [26] and the modified equation [49], respectively, are

$$v_{\rm cr} = 51.80 - 17.15(AR) + 0.72p_i$$
 (18)

$$v_{\rm cr} = p_i^{0.5} F_y^{0.2} \left(\frac{0.82}{\text{WFT}^{0.06}} + 0.49 \right)$$
 (19)

In order to use Eqs. (18) and (19), assumptions are required. For the NASA equation (Eq. (18)), the normal load on the wheel is considered to be 4000 N. Also, Horne et al. [26] provided a new equation for a 0.3 m passenger car tire based on 7.6 mm WFT on the road. Since Eqs. (18) and (19) are applicable for conditions in which the WFT is more than the depth of the tire tread, the half tread tire is used to validate both computer simulations. The critical speeds found by applying Eqs. (18) and (19) are 25.4 m/s and 24.0 m/s, respectively. Using the same condition with the FSI model for coupling the FE tire model with ABAQUS CFD, the critical speed is 23.3 m/s yielding 5.6% error with the empirical equation. Likewise, the FE tire model with STAR-CCM+ predicts a critical speed of 24.5 m/s with 2.7% error. The computational results from both FSI approaches show good agreement with the empirical equations.

Having verified the FSI models from both approaches by comparing the critical hydroplaning speed with empirical equations, the lift forces and cornering forces are examined. Different speeds and slip angles on the pavement with 5 mm WFT are examined for the lift and cornering forces. In addition to the treaded tire that is the main focus of this work, a bald tire is studied.

Figure 6 shows the tire pressure distribution, water splash, and transient development of the total lift force acting on the tire. Figure 6(a) presents the pressure of the fluid acting on the tire and

Table 3 Discretization error calculation using the grid convergence index [22]

Variable	STAR-CCM+	ABAQUS CFD
h_1, h_2, h_3	0.02, 0.03, 0.045 m	1.67,2.5,3.75 mm
$N_{\rm fine}, N_{\rm med}, N_{\rm coarse}$	1.58 m, 510 k, 148 k,	1.575 m, 470 k, 139 k
r_{21}, r_{32}	1.5	1.5
P	4.54	3.21
GCI ₂₃	8.4%	6.3%
GCI ₁₂	1.4%	1.6%

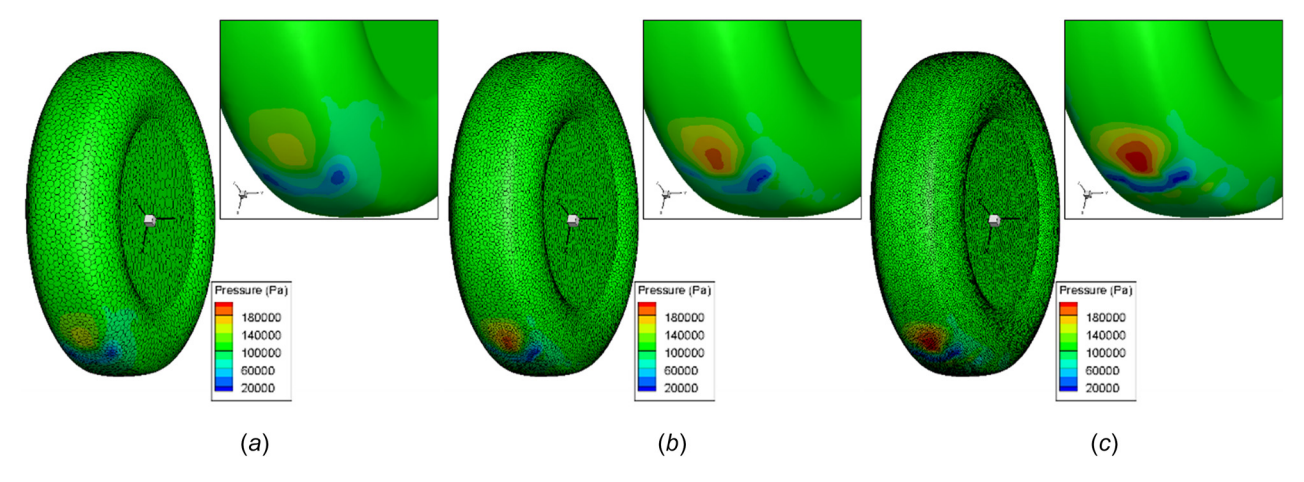


Fig. 5 Pressure and lift forces for bald tire with (a) coarse mesh, (b) medium mesh, and (c) fine mesh

the contact patch (marked as black edges). Most notable is that the contact patch is the region of the highest pressures and resulting when the water strikes the tire surface during the tire rotation. Pressure is also very high at the edges of the tire tread contacting the pavement. This could be because the tread pattern creates narrow channels for water to pass, which greatly increases the turbulence level of the fluid flow and increases the corresponding fluid pressure on the tire. Figures 6(c)-6(e) illustrates the time-dependent interaction between the water and the tire using an

isosurface of water volume fraction equal to 0.3 or larger. Water channels form at the front of the tire through the treads and is redirected to the sides of the tire as the tire rotates, which is represented as water splash. Figure 6(e) shows the lift force acting on the tire with time, where after $0.02 \, \text{s}$, the lift force asymptotes to a constant force. The negative value corresponds to the direction of the forces, which is acting to the opposite direction of the gravity force based on the coordinates defined in Fig. 2. The lift force shows a spike increase from $0 \, \text{s}$ to $0.005 \, \text{s}$ as water starts to build

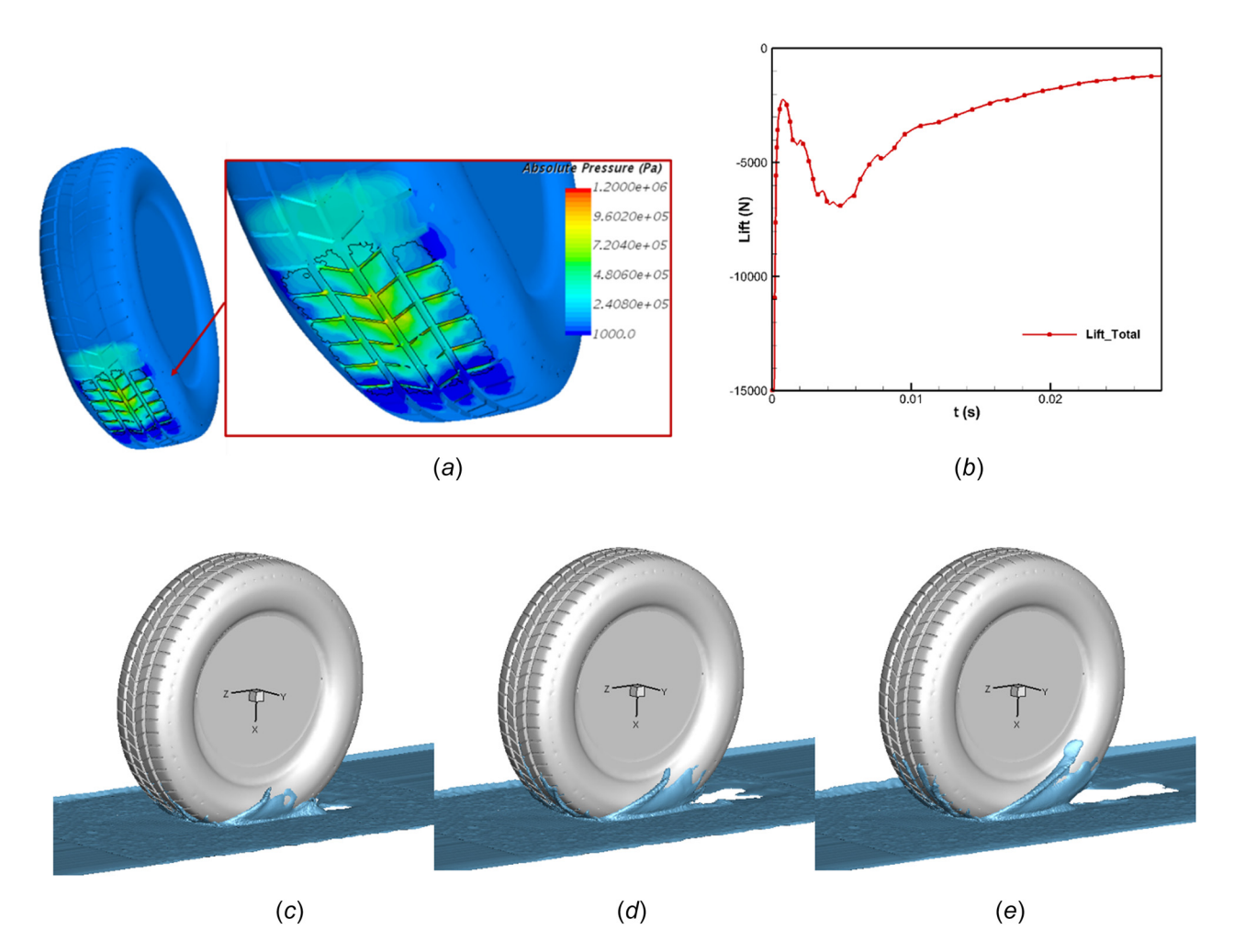


Fig. 6 Tread tire pressure results and water splash with two-way coupled model: (a) fluid pressure acting on the tread tire; (b)–(d) water splash along time at t = 0.01, 0.015, and 0.02 s; and (e) total lift force profile along time

up at the front edge of the contact area and below the tread. It then decreases since water gets discharged from the tread to the lateral sides

As shown in Fig. 7 for a bald tire and treaded tire, the lift forces predicted using the FE tire model with ABAQUS-CEL and STAR-CCM+ cosimulations increase with vehicle speed. Also, the lift force for bald tire reaches the saturated value at lower speeds, as expected. Generally, the results obtained from ABAQUS-CEL and integration of FE tire model with STAR-CCM+ are similar. The improvement with the STAR-CCM+ predictions can be associated with the more accurate turbulence model used to capture the behavior of the fluid at length scales smaller than the smallest element length in the CEL method.

As the lift force caused by the hydrodynamic pressure in the fluid domain changes, the cornering force of the tire also changes. In vehicle dynamics, the slip angle is the angle between the direction that the wheel is traveling and the direction that it is pointing. The net lateral force on each tire is generated by the lateral deformation of the tire surface, which is nominally zero at the leading edge and linearly increases until localized slip begins to occur. The location along the tire contact patch at which localized slip begins is dependent on the friction and the localized vertical force [50]. The capability to generate lateral forces is closely coupled with the ability to generate longitudinal forces (the total tractive force available being approximately equal to the vector sum of the two). Thus, as the lateral force increases, less longitudinal force is available for braking and thereby can significantly increase the hydroplaning risk. A schematic demonstrating slip is shown in Fig. 8.

In Figs. 9 and 10, the lateral force versus slip angle for 5 mm WFT at 17.8 and 22.4 m/s are presented, respectively. As shown in Fig. 9, the lateral force increases with slip angle up to a saturation limit at which the maximum available tractive force is reached. Wet conditions can have at least three detrimental effects on the ability to generate tractive forces. Specifically, at the tire-road contact patch, three things are reduced: the lift force created by the water film reduces the vertical force at the tire-road contact patch (reduced by the lift force exerted at the tire-water interface), the effective friction, and the size of the tire-road contact patch. Since the tire-road interface supports a shear force, but the tire-water interface does not, it is clear that the available lateral force saturates at lower slip angles as caused by the hydroplaning effect. These effects are exacerbated at higher speeds because both the size of the tire-road contact patch and its effective vertical force are reduced due to the increased size and lift force of the tire-water interface. For lateral forces obtained from the STAR-CCM+ cosimulation, the lateral force saturates at higher

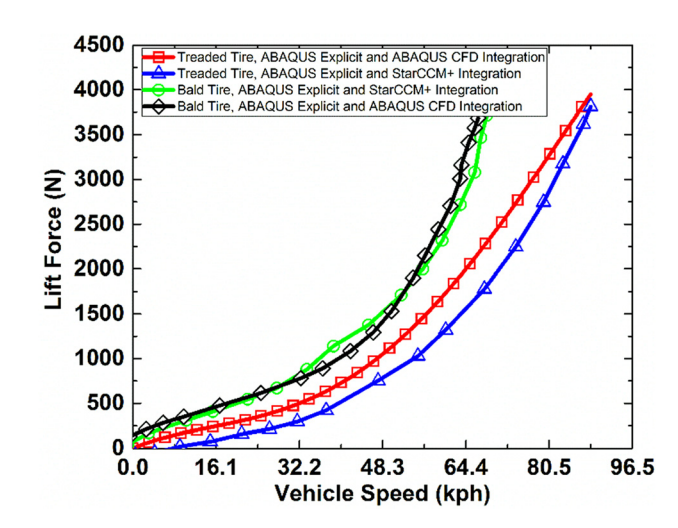


Fig. 7 Lift force obtained for treaded and bald tire, using different cosimulation methods

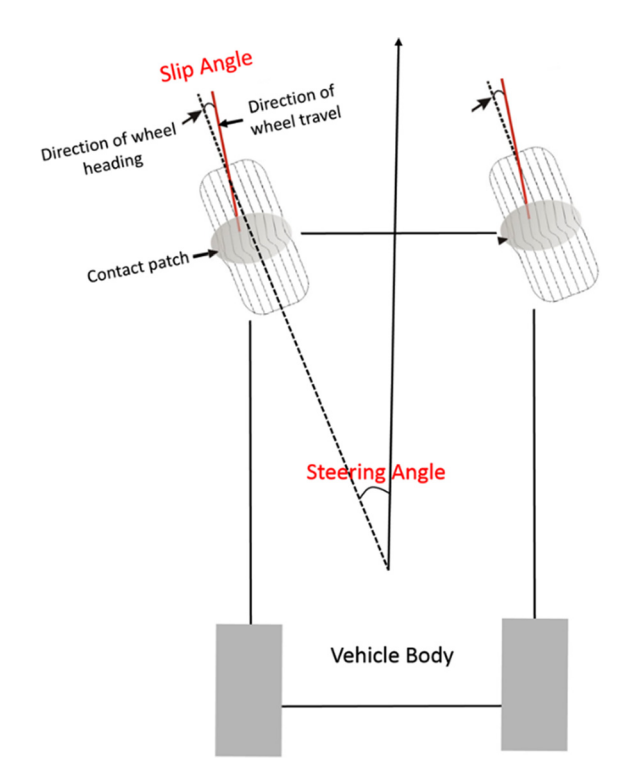


Fig. 8 Schematic of bald tire with slip angle

slip angles as compared to the ABAQUS-CEL model. This is due to slightly lower lift force captured through the cosimulation method using STAR-CCM+, which also incorporates a model for two-phase flow. For the dry condition, since there is no need to have the CFD code running in STAR CCM+, only the tire model in the ABAQUS Implicit is used.

The cornering force for treaded and bald tires using ABAQUS-CEL at 22.4 m/s is presented in Fig. 10 It is obvious that the effect of the lift force from hydroplaning is more significant at higher speeds. Accordingly, the tire reaches its cornering saturation at lower slip angles with lower corresponding lateral force. As expected, a lower lateral force for the bald tire as compared to the treaded tire is obtained, which is due to higher lift force caused by lack of presence of grooves for the bald tire. When a vehicle moves on wet pavement, the friction coefficient between tire and pavement is less than for dry conditions. In addition, as the

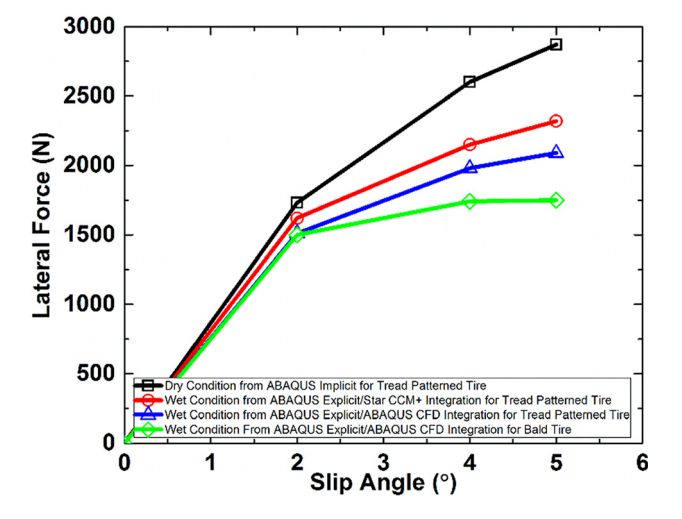


Fig. 9 Cornering force obtained for treaded and bald tire, using different cosimulation methods at 40

vehicle speed increases on wet pavement, the dynamic pressure induced by the water pushes the tire upward and increases the propensity to hydroplane.

The results from the simulations are compared with the experimental data provided by CALSPAN Tire Research Facility (TIRF) [51] shown in Fig. 11. Although the tire size tested by CALSPAN is different from that of this study, the experimental tests can be utilized to draw a comparison between the trend of lateral forces generated on wet and dry conditions. Based on the result provided in Ref. [51], the experimental results reveal that the peak lateral force at each slip angle in wet conditions is less than that of dry conditions. In addition, the difference between the lateral forces at dry and wet condition increase with slip angle, which has agreement with the simulation results in this work.

Figure 12 summarizes the water—tire interaction with the bald tire and the treaded tire under 0 deg and 2 deg slip angles and shows the water splash and spray. The fluid free surface is captured with the isosurface specified with a water volume fraction of 0.3. Comparing Figs. 12(a) and 12(b) of the water distribution between the bald tire and the treaded tire at 0 deg slip angle, both cases demonstrate that water splashes along the sides of the tire. However, the water distributions for the bald tire and treaded tire are very different. For the tread tire, it is clear that water separates

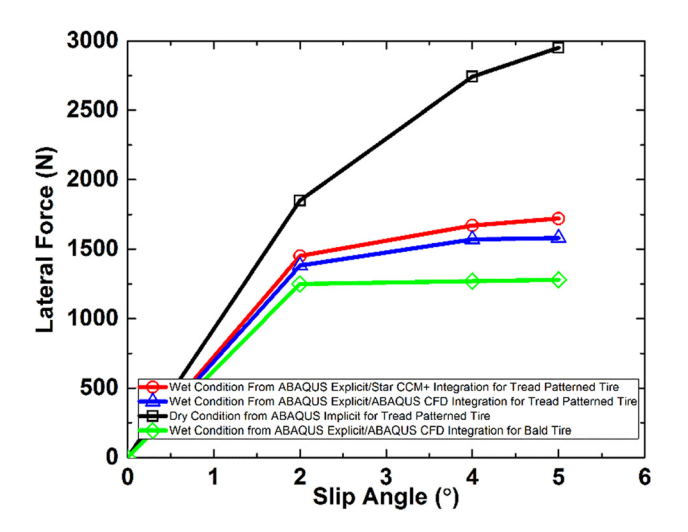


Fig. 10 Cornering force obtained for treaded and bald tire, using different cosimulation methods at 50 mph

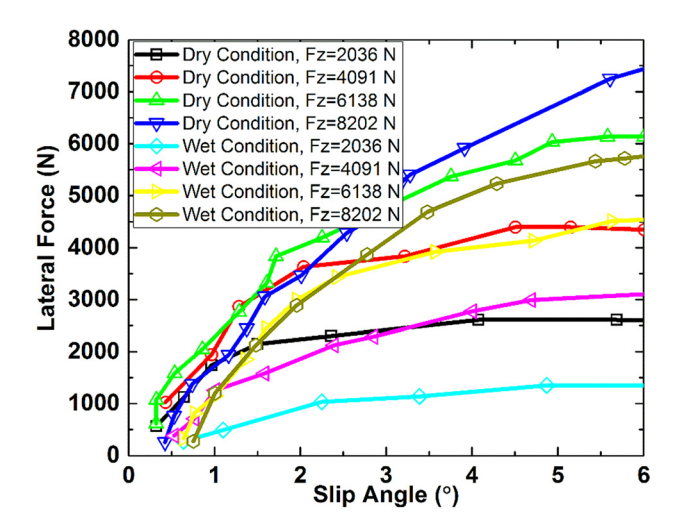
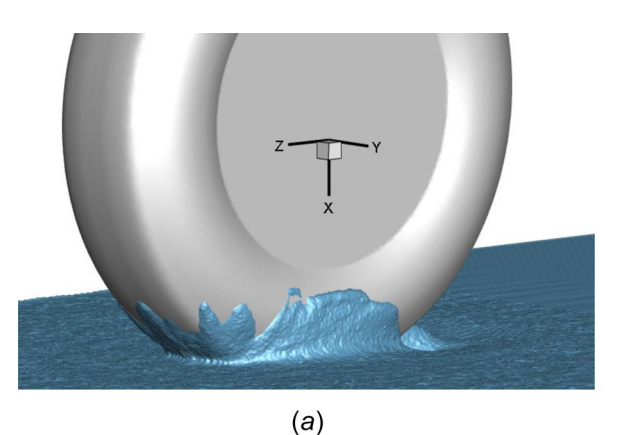
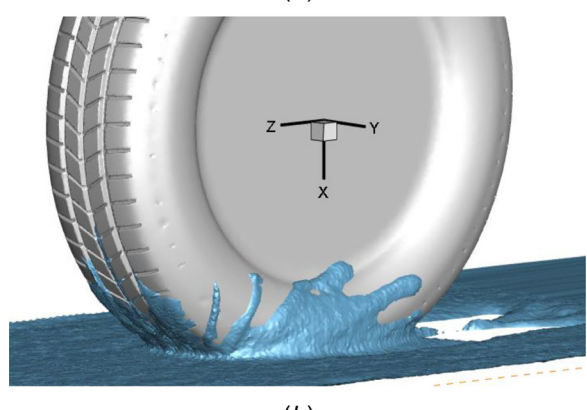


Fig. 11 Experimental data of the cornering forces for wet and dry conditions at different weight loads

into streams and is displaced with the tire grooves, which is not observed with the bald tire. When roads are wet, tire grooves channel water away, which helps prevent tires from hydroplaning, unlike the bald tire scenario where the traction is reduced and hydroplaning occurs more readily.

The effect of slip angle on water splash is demonstrated in Fig. 12(c), whereby the water splash is more significant along the side of the tire, whereby the lateral force increases, as shown in Figs. 9 and 10. More streams of water have been squeezed out of the tire to ensure a good contact between tire and ground because of the tire tread. Comparing between Figs. 12(b) and 12(c) with different slip angles, the addition of slip angle has greatly increased the water splash on the tire side. Since the force along the lateral direction caused by such water splash is only a small portion of the force generated laterally due to the tire–pavement interaction and slip angle, the cornering forces because of the slip angle are mainly studied from the output in the tire–pavement FE model.





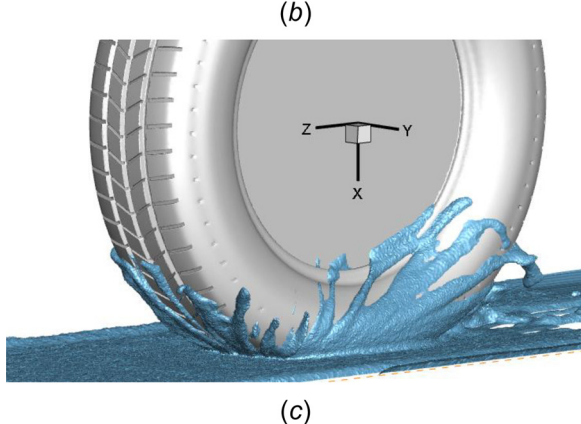


Fig. 12 Isosurface of water volume fraction of 0.3 showing water splash in (a) bald tire with 0 deg slip angle, (b) tread tire with 0 slip angle, and (c) tread tire with 2 deg slip angle

4 Conclusions

In this work, two different approaches were developed to study the effect of hydroplaning on lift and cornering forces for a passenger car tire. Both approaches were verified with empirical equations and compared well overall. It was shown that the new approach using ABAQUS and STAR-CCM+ cosimulation had slightly better agreement with the empirical models showing a 2.9% improvement. Also, the lateral forces obtained from simulation show a good agreement with the experiment data reported in the literature. It is noteworthy to mention that the new approach using STAR-CCM+ needs more computation time and memory; however, with the advent of supercomputers, it can be more applicable for future hydroplaning simulations. In addition, in the new hydroplaning modeling approach, free surface flow with moving boundaries to build and track the amount of water as well as the volume fraction of other fluids can be captured, which can be used to study tire tread design and its relationship to water splashing and aerodynamics [52].

Acknowledgment

The authors acknowledge the National Cooperative Highway Research Program (NCHRP) for continuous support of this research. The authors also acknowledge Center for Computing Research (CCR) at University at Buffalo, Center for Tire Research (CenTiRe) and Advanced Research Computing (ARC) at Virginia Tech for providing computational resources and technical support that have contributed to the results reported within this paper.

Nomenclature

 A_t = tire face area

AR = contact patch aspect ratio

b = body force

 $C_{10} = \text{constant describing the shear modulus } G = G/2$

d = displacement

 $D_1 =$ constant describing the bulk modulus $K = 2/\kappa$

e =energy density

E = total energy

 E_H = specific energy per unit mass

f =vertical component of tire force

 F_{v} = vertical load of vehicle on the tire

g = gravity

 G_k = turbulence kinetic energy generation

 $G_{\omega} =$ specific dissipation rate generation

h = grid size

I = the invariant of the deviatoric strain tensor

 $\overline{J_{e1}}$ = the elastic volume ratio

k = turbulence kinetic energy

 $k_{\rm eff} = =$ effective thermal conductivity

N =total number of grid cells

 n_f = vertical unit vector

p =fluid pressure

P = apparent order of accuracy

 $p_H = \tilde{\text{Hugoniot}}$ pressure

 $p_i = \text{inflation pressure}$

r = grid refinement factor

Re = Reynolds number

S = strain rate magnitude

 T_f = stress tensor exerted on the tire surface area

 \vec{v} = fluid velocity

 $v_{\rm cr}$ = hydroplaning critical speed

 $V_{\text{tire}} = \text{vehicle speed}$

W = strain energy potential (density) or stored energy function defined per unit volume

 $W_{\rm tire} = {\rm tire \ width}$

 Y_k = dissipation of turbulence kinetic energy

 Y_{ω} = dissipation of specific rate

Greek Symbols

 α = damping coefficient for turbulent viscosity

 Γ = effective diffusive rate

 μ_t = turbulent eddy-viscosity

 $\dot{\rho}$ = fluid density

 σ = Cauchy stress

 $\bar{\bar{\tau}} = \text{fluid stress tensor}$ $\phi = \text{volume fraction}$

 $\omega =$ specific dissipation rate

Subscripts/Superscripts

a = air

p =pressure force

s =shear force

w = water

References

- Fwa, T., Pasindu, H., and Ong, G., 2012, "Critical Rut Depth for Pavement Maintenance Based on Vehicle Skidding and Hydroplaning Consideration," J. Transp. Eng., 138(4), pp. 423–429.
- [2] Fwa, T. F., Kumar, A., and Ong, G. P., 2010, "Relative Effectiveness of Grooves in Tire and Pavement in Reducing Vehicle Hydroplaning Risk," Transp. Res. Rec., 2155(1), pp. 73–81.
- [3] Allbert, B., 1968, "Tires and Hydroplaning," SAE Paper No. 680140.
- [4] Matthies, H. G., and Steindorf, J., 2003, "Partitioned Strong Coupling Algorithms for Fluid–Structure Interaction," Comput. Struct., **81**(8–11), pp. 805–812
- [5] Walhorn, E., Hübner, B., and Dinkler, D., 2002, "Space-Time Finite Elements for Fluid-Structure Interaction," Proceedings in Applied Mathematics and Mechanics (PAMM), Augsburg, Germany, pp. 81–82.
- [6] Kim, T.-W., and Jeong, H.-Y., 2010, "Hydroplaning Simulations for Tires Using FEM, FVM and an Asymptotic Method," Int. J. Automot. Technol., 11(6), pp. 901–908.
- [7] Vincent, S., Sarthou, A., Caltagirone, J.-P., Sonilhac, F., Février, P., Mignot, C., and Pianet, G., 2011, "Augmented Lagrangian and Penalty Methods for the Simulation of Two-Phase Flows Interacting With Moving Solids. Application to Hydroplaning Flows Interacting With Real Tire Tread Patterns," J. Comput. Phys., 230(4), pp. 956–983.
- [8] Ong, G., and Fwa, T. F., 2007, "Effectiveness of Transverse and Longitudinal Pavement Grooving in Wet-Skidding Control," Transp. Res. Rec., 2005(1), pp. 172–182.
- [9] Menter, F., 1993, "Zonal Two Equation k-w Turbulence Models for Aerodynamic Flows," AIAA Paper No. 93-2906.
- [10] Menter, F. R., 1994, "Two-Equation Eddy-Viscosity Turbulence Models for Engineering Applications," AIAA J., 32(8), pp. 1598–1605.
- [11] Guo, X-X., Zhang, C., Cui, B-X., Wang, D., and Tsai, J., 2013, "Analysis of Impact of Transverse Slope on Hydroplaning Risk Level," Procedia-Soc. Behav. Sci., 96, pp. 2310–2319.
- [12] Zhou, H. C., Wang, G. L., Yang, J., and Xue, K. X., 2014, "Numerical Simulation of Tire Hydroplaning and Its Influencing Factors," Appl. Mech. Mater., 602–605, pp. 580–585.
- [13] Menter, F. R., Kuntz, M., and Langtry, R., 2003, "Ten Years of Industrial Experience With the SST Turbulence Model," *Turbulence, Heat and Mass Transfer*, Vol. 4, K. Hanjalic, Y. Nagano, and M. Tummers, eds., Begell House, Danbury, CT, pp. 625–632.
- [14] Dong, B., Zhang, L., Chen, M., Tang, B., and Liu, T., 2013, "Influencing Factor of Hydrodynamic Pressure on Tire in Wet Weather Based on Fluent," J. Highw. Transp. Res. Dev., 7(1), pp. 98–104.
- Transp. Res. Dev., 7(1), pp. 98–104.
 [15] Liang, X., Li, W., Fan, W., and Zhao, G., 2014, "Numerical Simulation and Hydrodynamic Performance Prediction for Hydroplane Longitudinal Motion," Comput. Model. New Technol., 18(2), pp. 27–32.
- [16] Liu, T. Z., Tang, B. M., Dong, B., and Gao, J. P., 2012, "Analysis of Impact of Tire Tread Groove Depth on Hydroplaning Risk Level," Adv. Mater. Res., 455–456, pp. 1459–1467.
- [17] Ong, G., and Fwa, T. F., 2006, "Transverse Pavement Grooving Against Hydroplaning—I: Simulation Model," J. Transp. Eng., 132(6), pp. 441–448.
 [18] Nazari, A., and Nazari, A., "Experimental Investigation on Newtonian Drop
- [18] Nazari, A., and Nazari, A., "Experimental Investigation on Newtonian Drop Formation in Different Continuous Phase Fluids," ASME Paper No. IMECE2018-86602.
- [19] Nazari, A., Zadkazemi Derakhshi, A., Nazari, A., and Firoozabadi, B., 2018, "Drop Formation From a Capillary Tube: Comparison of Different Bulk Fluid on Newtonian Drops and Formation of Newtonian and Non-Newtonian Drops in Air Using Image Processing," Int. J. Heat Mass Transfer, 124, pp. 912–919.
- [20] Koishi, M., Oskano, T., Olovsson, L., Saito, H., and Makino, M., 2001, "Hydroplaning Simulation Using Fluid-Structure Interaction in LS-DYNA," Proceeding of the Third European LS-DYNA Users Conference, Paris, France.
- [21] Cho, J. R., Lee, H. W., Sohn, J. S., Kim, G. J., and Woo, J. S., 2006, "Numerical Investigation of Hydroplaning Characteristics of Three-Dimensional Patterned Tire," Eur. J. Mech. A, 25(6), pp. 914–926.
- [22] Seta, E., Nakajima, Y., Kamegawa, T., and Ogawa, H., 2000, "Hydroplaning Analysis by FEM and FVM: Effect of Tire Rolling and Tire Pattern on Hydroplaning," Tire Sci. Technol., 28(3), pp. 140–156.

- [23] Cho, J. R., Lee, H. W., and Yoo, W. S., 2007, "A Wet-Road Braking Distance Estimate Utilizing the Hydroplaning Analysis of Patterned Tire," Int. J. Numer. Methods Eng., 69(7), pp. 1423-1445.
- [24] Bathe, K. J., and Zhang, H., 2004, "Finite Element Developments for General Fluid Flows With Structural Interactions," Int. J. Numer. Methods Eng., 60(1), pp. 21-32.
- [25] Wang, H., Al-Qadi, I. L., and Stanciulescu, I., 2012, "Simulation of Tyre-Pavement Interaction for Predicting Contact Stresses at Static and Various Rolling Conditions," Int. J. Pavement Eng., 13(4), pp. 310-321.
- [26] Horne, W. B., Yager, T. J., and Ivey, D. L., 1986, "Recent Studies to Investigate Effects of Tire Footprint Aspect Ratio on Dynamic Hydroplaning Speed," The Tire Pavement Interface, ASTM International, West Conshohocken, PA.
- [27] Systemes Simulia Corporation, 2014, "Abaqus V. 6.14 Documentation," Dassault Systemes Simulia Corporation, Providence, RI.
- [28] Yamashita, H., Matsutani, Y., and Sugiyama, H., 2015, "Longitudinal Tire Dynamics Model for Transient Braking Analysis: ANCF-LuGre Tire Model," ASME J. Comput. Nonlinear Dyn., **10**(3), p. 031003.
- [29] Yamashita, H., Jayakumar, P., and Sugiyama, H., 2016, "Physics-Based Flexible Tire Model Integrated With Lugre Tire Friction for Transient Braking and Cornering Analysis," ASME J. Comput. Nonlinear Dyn., 11(3), p. 031017.
- [30] Liang, C., Ji, L., Mousavi, H., and Sandu, C., 2019, "Evaluation of Tire Traction Performance on Dry Surface Based on Tire-Road Contact Stress," Proceedings of SIAR International Congress of Automotive and Transport Engineering: Science and Management of Automotive and Transportation Engineering, Romania, pp. 138-152.
- [31] Gent, A., 1992, Elasticity, in Engineering With Rubber, Hanser, München, Germany
- [32] Kang, Y-S., Nazari, A., Chen, L., Ferris, J. B., Taheri, S., Battaglia, F., and Flintsch, G., 2019, "A Probabilistic Approach to Hydroplaning Potential and
- Risk," SAE Int. J. Passenger Cars: Mech. Syst., 12(1), pp. 63–70.
 [33] Nazari, A., Chen, L., Battaglia, F., and Taheri, S., "Developing an Advance Tire Hydroplaning Model Using Co-Simulation of Fully Coupled FEM and CFD Codes to Estimate Cornering Force," ASME Paper No. IMECE2018-
- [34] Muzaferija, S., 1998, "Computation of Free Surface Flows Using Interface-Tracking and Interface-Capturing Methods," *Nonlinear Water-Wave Interac*tion, Computational Mechanics, Southampton, UK.
- [35] Ong, G. P., 2006, "Hydroplaning and Skid Resistance Analysis Using Numerical Modeling," Doctoral thesis, National University of Singapore, Singapore.
- [36] Ong, G., and Fwa, T. F., 2007, "Prediction of Wet-Pavement Skid Resistance and Hydroplaning Potential," J. Transp. Res. Board, 2005(1), pp. 160-171.

- [37] Ong, G., and Fwa, T. F., 2008, "Modeling and Analysis of Truck Hydroplaning
- on Highways," J. Transp. Res. Board, **2068**(1), pp. 99–108. Browne, A. L., 1971, "Dynamic Hydroplaning of Pneumatic Tires," Doctoral
- thesis, Northwestern University, Evanston, IL. [39] Browne, A. L., 1975, "Mathematical Analysis for Pneumatic Tire Hydroplaning," Surface Texture Versus Skidding, ASTM International, West Conshohocken, PA, pp. 75-94.
- [40] Horne, W. B., and Joyne, U. T., 1965, "Pneumatic Tire Hydroplaning and Some Effects on Vehicle Performance," SAE Paper No. 650145.
- Moore, D. F., 1966, "Prediction of Skid Resistance Gradient and Drainage Characteristics for Pavements," Highway Research Record.
- [42] Baudille, R., and Biancolini, M. E., 2005, "Modelling FSI Problems in Fluent: A General Propose Approach by Means of UDF Programming," Proceeding of the European Automotive CFD Conference, Frankfurt, Germany.
- Yamashita, H., Jayakumar, P., Alsaleh, M., and Sugiyama, H., 2018, "Physics-Based Deformable Tire-Soil Interaction Model for Off-Road Mobility Simulation and Experimental Validation," ASME J. Comput. Nonlinear Dyn., 13(2), p. 021002.
- [44] Dassault Systemes, 2016, "Abaqus V. 6.14, Online Documentation Help, Theory Manual," Dassault Systemes, Providence, RI.
- [45] Sillem, A., 2008, "Feasibility Study of a Tire Hydroplaning Simulation in a Monolithic Finite Element Code Using a Coupled Eulerian-Lagrangian Method," Delft Institute of Applied Mathematics, Delft, The Netherlands.
- [46] Noh, W. F., 1963, "CEL: A Time-Dependent, Two-Space-Dimensional, Coupled Eulerian-Lagrange Code," Lawrence Radiation Lab., University of California, Livermore, CA, Report No. UCRL-7463.
- Trulio, J. G., 1966, "Theory and Structure of the AFTON Codes," Nortronincs, Newbury Park, CA.
- [48] Celik, I. B., Ghia, U., and Roache, P. J., 2008, "Procedure for Estimation and Reporting of Uncertainty Due to Discretization in CFD Applications," ASME J. Fluids Eng., 130(7), p. 078001.
- [49] Gunaratne, M., Lu, Q., Yang, J., Jayasooriya, W., Yassin, M., and Amarasiri, S., 2012, "Hydroplaning on Multi Lane Facilities," Florida Department of Transportation, Tallahassee, FL.
- [50] Okano, T., and Koishi, M., 2001, "A New Computational Procedure to Predict Transient Hydroplaning Performance of a Tire," Tire Sci. Technol., 29(1), pp. 2-22.
- Salaani, M. K., Heydinger, G. J., and Grygier, P. A., 2006, "Measurement and Modeling of Tire Forces on a Low Coefficient Surface," SAE Paper No. 0148-7191.
- [52] Co, T. Y. R., 2015, "Yokohama Rubber Advancing Tire Aerodynamics Technology. New Advances Reduce Vehicle Aerodynamic Drag and Lift," The Yokohama Rubber Co., Ltd., Japan, accessed June 8, 2020, https://www. y-yokohama.com/release/?id=2518&lang=en&sp=40